IOP Publishing Journal of Geophysics and Engineering
J. Geophys. Eng. **14** (2017) 120–131 (12pp) doi:10.1088/1742-2140/14/1/120

Comparison analysis of fractal characteristics for tight sandstones using different calculation methods

Xiaoyang Zhang[1,2,3], **Caifang Wu**[1,2] **and Teng Li**[1,2]

[1] Key Laboratory of Coalbed Methane Resource and Reservoir Formation Process, Ministry of Education, Xuzhou 221008, People's Republic of China
[2] School of Resources and Geosciences, China University of Mining & Technology, Xuzhou 221008, People's Republic of China

E-mail: zhanglsyr@cumt.edu.cn and caifangwu@sina.com

Received 19 June 2016, revised 31 October 2016
Accepted for publication 8 November 2016
Published 19 December 2016

Abstract

The micropore structure of a tight sandstone is the decisive factor in determining its reserve and seepage characteristics. An accurate description of the pore structures and a complete characterization of the gas–water permeability are critical when exploring for tight sandstone gas. One simple and effective way to quantitatively characterize the heterogeneity and complexity of the pore structures in a low permeability reservoir is the fractal dimension. In this study, three different methods, each utilizing mercury intrusion porosimetry (MIP) data, were adopted to analyze the fractal dimensions and the fractal curves of sandstones from the no. 8 layer of the Xiashihezi Formation (He 8 member) in the Linxing block, dated from the Middle Permian. The morphological features of the fractal curves, the characteristics of the fractal dimensions and the theoretical differences between these three methods were also discussed. The results show that the fractal dimensions obtained by method I reflect the characteristics of the remaining pores that are not intruded by mercury, and they show that the involved pore scales are more comprehensive. While in methods II and III, both obtain the fractal dimensions of the pores intruded by mercury, the difference between them is in the selection of a simplified pore shape model, which results in the fractal dimensions differing by a value of 1 between them. No matter which method is adopted, the pore structures of tight sandstone reservoirs in the Linxing block exhibit fractal characteristics. However, the fractal dimensions obtained by method I are more suitable for describing the complexity and petrophysical properties of the tight sandstone pores in the He 8 member of the Linxing block. The fractal curves obtained by different methods are consistent to a certain extent in terms of morphological changes. Small pores ($<r_{\text{max-point}}$) usually demonstrate more fractal characteristics, while large pores ($>r_{\text{max-point}}$) are the critical factor affecting the seepage characteristics of the reservoir.

Keywords: tight sandstone, pore structure, fractal dimension, fractal curve

(Some figures may appear in colour only in the online journal)

1. Introduction

Tight sandstone gas is a non-conventional natural gas resource that accumulates in low porosity and low permeability sandstones (Holditch 2006, Zou *et al* 2012, Guo *et al* 2016). There are large scale reserves of tight sandstone gas widely distributed across China which provide a critical supplement to the current conventional oil and gas resources. The amount of technically recoverable reserves of tight sandstone gas in China is estimated to be 9200 ~ 13 400 billion m^3 (Xie *et al* 2014, Jiang *et al* 2015). Gas is mainly accumulated in the pore space of tight sandstones and the

[3] Author to whom any correspondence should be addressed.

micropore structure is the decisive factor affecting the reservoir properties and seepage characteristics (Lai and Wang 2015). As tight sandstone reservoirs generally have experienced complicated diagenesis and tectonic processes, great depth, high diagenesis intensity, tight lithology, complicated pore structure and strong heterogeneity are all typical features of these reservoirs. Such complicated features make it difficult to accurately describe a reservoir's pore structure using traditional methods (Morad *et al* 2010, Clarkson *et al* 2012, Zou *et al* 2012, Lai and Wang 2015, Xiao *et al* 2016).

Previous studies have shown that the fractal dimension can be used to represent the roughness of a solid surface or a pore wall. As a simple and effective parameter, the fractal dimension has been widely used to quantitatively characterize the complexity of the pore structure of low permeability reservoirs, such as sandstone, coal and shale reservoirs (Krohn 1988a, 1988b, Angulo and Gonzalez 1992, Fu *et al* 2005, Yao *et al* 2009, Li 2010, Yang *et al* 2014). Since Mandelbrot first defined fractal geometry, many scholars have proven that the pores of low permeability reservoirs have fractal characteristics that can be described with fractal theory. Katz and Thompson (1985) used scanning electron microscopy and optical data to show that the pore spaces of several sandstones were fractal geometries. Wong *et al* (1986) studied the microstructure of sedimentary through small-angle neutron scattering, and found the fractal characters of pore surfaces.

At present, the pore structure of a reservoir is usually characterized by mercury intrusion porosimetry (MIP). MIP could obtain the parameters related to the pore structure, such as the maximum intrusive mercury saturation, the displacement pressure, the efficiency of mercury ejection and the pore throat radius (León y León 1998, Ziarani and Aguilera 2012, Gao and Hu 2013, Zhu *et al* 2015). According to the MIP data and fractal geometry theory, there are many different methods for calculating fractal dimension. Friesen and Mikula (1987) determined the fractal dimension using the data of pore volume and the capillary pressure (their calculation formula is in accordance with method III below). For the coals, three pressure regimes were indicated by distinct values of fractal dimension, and the fractal dimension for the porous surfaces ranged from 2.6–3 (Friesen and Mikula 1987). Pérez Bernal and Bello López (2000) also used this approach to analyze the fractal characteristics for building stone. It has been demonstrated that the pore surface was fractal in pore diameters ranging from 0.012–100 μm, and the fractal dimension increased in weathered stones from 2.44–2.62. He and Hua (1998) derived a calculation method (method I, see below) using the data of the intrusive mercury saturation and the capillary pressure from MIP. They indicated that the pore distribution in sandstones was statistically self-similar when the pore radius ranged from 0.2–50 μm, and the fractal dimension ranged from 2.41–2.63. In addition, according to the fractal structures and properties of reservoir pores, they also derived fractal geometric formulas describing the relative permeability of the wetting phase and non-wetting phase based on the Burdine model (Burdine 1953), which achieved an easier convert between the capillary pressure curve and the relative permeability curve. Li and Horne (2003) proposed a model (method II, see below) to calculate the fractal dimension and characterize the heterogeneity for Geysers rock and Berea sandstone. The calculated values of the fractal dimension for all samples were in a range from 2–3. Lai and Wang (2015) found that the fractal dimension was mainly associated with micropores for tight gas sandstones, and the small pores tended to have fractal dimension values less than 2.5, while the large pores had values larger than 3.

Previous scholars usually believed that the micropores of sandstone reservoirs have obvious fractal characteristics described by a fractal dimension ranging from 2–3; the fractal dimension upper 3 corresponds to a totally irregular or rough surface (Pfeifer and Avnir 1983, Li 2010, Lai and Wang 2015). Greater fractal dimension has been shown to correspond to rougher pore throat surfaces, poorer sorting, more complicated pore size distributions, poorer reserving performance and stronger heterogeneity in reservoirs (Shen and Li 1995, Li and Horne 2006, Li 2010).

After summarizing the study of previous scholars, there have been three main methods (method I, method II and method III, see below) to obtain the fractal dimension using mercury intrusion techniques. Most studies selected only one method to analyze the fractal characteristics of pore structures; there has rarely been a study on the similarities and differences of calculating the fractal dimension by different methods. In this paper, based on MIP data from tight sandstones of the He 8 member in the Linxing block on the eastern margin of the Ordos Basin, the pore features have been analyzed and the pore structures have been classified with three different methods. The fractal dimensions and the fractal curves obtained by these methods are then compared. The intrinsic theoretical difference among the three methods is discussed, and the corresponding relationship between the morphological changes of the fractal curves is then analyzed.

2. Materials and methods

2.1. Methodology

Presently, the fractal dimension can be calculated from experimental MIP data with three approaches, which are referred to as method I, method II and method III in this paper.

(1) Method I

According to the theory of fractal geometry, if the pore size distribution displays fractal characteristics, the pore number $N(>r)$ of pores with a radius greater than r can be expressed as:

$$N(>r) = \int_r^{r_{\max}} P(r)\mathrm{d}r = ar^{-D} \tag{1}$$

where $r_{\max}$ is the maximum pore radius in the reservoir, $P(r)$ is the pore size distribution density function, a is a proportional constant, and D is the fractal dimension.

By taking the derivative of N with respect to r, equation (2) could be computed from equation (1):

$$P(\mathrm{r}) = \frac{\mathrm{d}N(>r)}{\mathrm{d}r} = a'r^{-D-1}. \quad (2)$$

The integration of equation (2) results in the accumulated pore volume of pores with a radius less than r in the reservoir, $V(<r)$, as expressed in equation (3):

$$V(<r) = \int_{r_{\min}}^{r} P(r)\alpha r^3 \mathrm{d}r = a''(r^{3-D} - r_{\min}^{3-D}) \quad (3)$$

where $a'' = a'\alpha/(3-D)$, α is a constant associated with the shape of the pores, and $r_{\min}$ is the minimum pore radius in the reservoir.

Similarly, the total pore volume of all pores in the reservoir yields:

$$V = a''(r_{\max}^{3-D} - r_{\min}^{3-D}). \quad (4)$$

Combining equations (3) and (4):

$$S = \frac{V(<r)}{V} = \frac{r^{3-D} - r_{\min}^{3-D}}{r_{\max}^{3-D} - r_{\min}^{3-D}}. \quad (5)$$

As $r_{\min}$ is much smaller than $r_{\max}$ and r, equation (5) can be simplified into equation (6):

$$S = \left(\frac{r}{r_{\max}}\right)^{3-D}. \quad (6)$$

Considering a capillary tube model, the capillary pressure can be expressed as follows:

$$P_{\mathrm{c}} = \frac{2\sigma\cos\theta}{r} \quad (7)$$

where P_{c} is the capillary pressure MPa, σ is the surface tension mN/m, and θ is the contact angle °.

Substituting equation (7) into equation (6):

$$S = \left(\frac{P_{\mathrm{c}}}{P_{\min}}\right)^{D-3} \quad (8)$$

where $P_{\min}$ is the capillary pressure which corresponds to $r_{\max}$, in MPa. S is known as the wetting phase saturation, in %.

Taking the log of equation (8) gives:

$$\lg S = (D-3)\lg P_{\mathrm{c}} + (3-D)\lg P_{\min} \quad (9)$$

which can be rearranged into equation (9):

$$\lg(1 - S_{\mathrm{Hg}}) = (D-3)\lg P_{\mathrm{c}} + (3-D)\lg P_{\min} \quad (10)$$

where S_{Hg} is the cumulative mercury saturation expressed as a percentage.

The fractal dimension can then be derived by plotting the double logarithm of 1-S_{Hg} and P_{c}, where the fractal dimension will be the slope of the straight lines.

(2) Method II

According to the capillary tube method and the definition of fractal geometry, the number of the units $N(r)$ can be represented mathematically by a power-law function:

$$N(r) = \frac{V_{\mathrm{Hg}}}{\pi r^2 l} \propto r^{-D} \quad (11)$$

where l is the length of a capillary, V_{Hg} is the cumulative volume of mercury at a certain capillary pressure, and D is the fractal dimension.

Equation (12) can be obtained from equation (11):

$$V_{\mathrm{Hg}} \propto r^{2-D}. \quad (12)$$

This expression can be combined with the Laplace law:

$$P_{\mathrm{c}} = \frac{2\sigma\cos\theta}{r} \quad (13)$$

where P_{c} is the capillary pressure MPa, σ is the surface tension mN/m, and θ is the contact angle °.

Substituting equation (13) into equation (2):

$$V_{\mathrm{Hg}} \propto P_{\mathrm{c}}^{-(2-D)}. \quad (14)$$

The definition of mercury saturation can be calculated as follows:

$$S_{\mathrm{Hg}} = V_{\mathrm{Hg}}/V_{\mathrm{P}} \quad (15)$$

where V_{P} is the total pore volume, S_{Hg} is the cumulative mercury saturation expressed as a percentage.

Combining equations (14) and (15) gives:

$$S_{\mathrm{Hg}} = \alpha P_{\mathrm{c}}^{-(2-D)} \quad (16)$$

where α is a constant.

Similar to method I, the fractal dimension D can then be derived by plotting the double logarithm of S_{Hg} and P_{c} and measuring the slope.

(3) Method III

If the pore shape can be treated as a sphere, equation (17) can be inferred from equation (4):

$$V_{\mathrm{Hg}} \propto P_c^{-(3-D)}. \quad (17)$$

Differentiating equation (17) yields:

$$\frac{\mathrm{d}V_{\mathrm{Hg}}}{\mathrm{d}P_{\mathrm{c}}} \propto P_{\mathrm{c}}^{D-4}. \quad (18)$$

Following the same procedure, the fractal dimension can be calculated by plotting the double logarithm of $\mathrm{d}V_{\mathrm{Hg}}/\mathrm{d}P_{\mathrm{c}}$ and P_{c}. It is also possible to infer equation (18) with other methods (Li *et al* 1999, Fu *et al* 2005, Li 2010).

2.2. Experimental measurements

Linxing block is situated in Lin County and Xing County of the western Shanxi Province, on the Yishan slope belt and the Jinxi flexural fold belt of the Ordos Basin (figure 1). The coal strata of the Linxing block are developed in a transitional facies, and the sandstone reservoirs are multi-layered and widely distributed. In the Linxing block, many exploratory wells are drilled into tight sandstone gas reservoirs, and the Taiyuan Formation and the Xiashihezi Formation produce industrial gas flow. The no. 8 layer of the Xiashihezi Formation (He 8 member) is the major stratum for tight sandstone gas exploration and development in the research area, and has an average effective reservoir thickness of 13.56 m. All of the coring samples were collected from the He 8 member of the Linxing block from the Middle Permian. Twenty-five sandstone samples were selected using an AutoPoreIV 9505 porosity analyzer to measure the pore

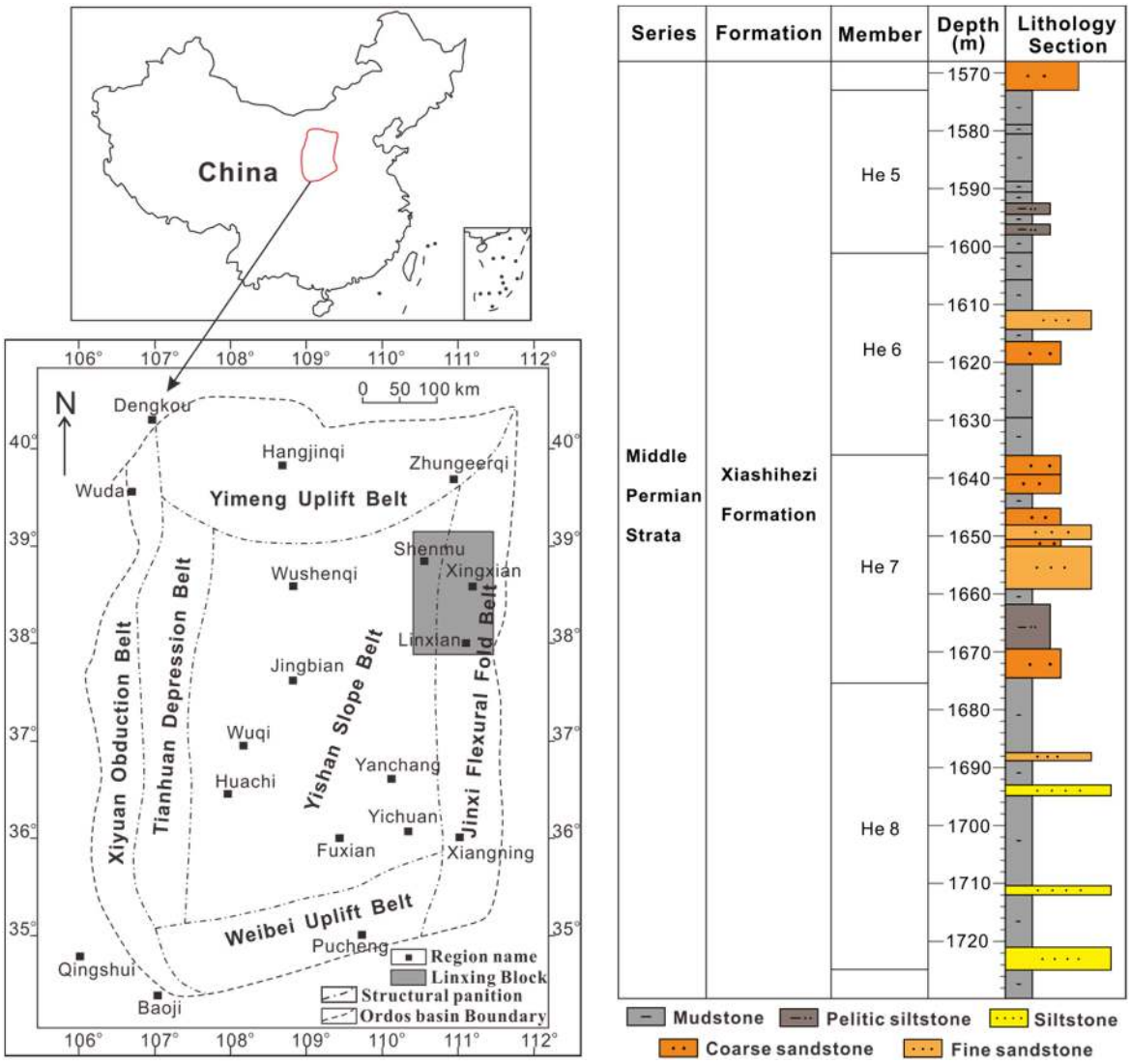

Figure 1. Map showing the location of the Linxing block and the stratigraphy of the Xiashihezi Formation.

characteristics. The maximum measuring pressure is 101.32 MPa, with an air/mercury surface tension of 480 mN m^{-1}. The contact angle of the mercury phase is 140°, and the representation range of this porosity analyzer is from 7 nm–105 μm.

3. Results and discussion

3.1. Pore structure characteristics

The mercury intrusion porosimetry analysis of the 25 sandstone samples in the Linxing block indicates that the sandstone porosity ranges from 4.62%–12.70% with an average of 8.26%, while the air permeability ranges from 0.05×10^{-3} to 1.96×10^{-3} μm^2, with an average of 0.34×10^{-3} μm^2. Most pores are tiny, with an average pore radius between 0.14 and 0.62 μm, averaging 0.29 μm. The r_{35} (pore radius corresponding to 35% mercury saturation) ranges from 0.01–0.79 μm and averages 0.17 μm. The maximum mercury saturation fluctuates between 36.16% and 96.83% with an average of 75.80%. The efficiency of mercury withdrawal averages 35.23% and ranges from 27.20%–46.94% (table 1). In conclusion, the He 8 member sandstones in the Linxing block are typically tight sandstone reservoirs presenting low porosity, low permeability and complex pore structures. According to mercury injection capillary curve shapes, the pore structures can be divided into four types, which are represented by samples 6-1, 4-3, 4-5 and 4-7 (table 2, figure 2).

The maximum intrusive mercury saturation decreases from type I to type IV as the average pore radius decreases, while at the same time the displacement pressure increases and the capillary pressure curve turns from coarse type to fine type. The pore throat sizes of the representative samples are mainly distributed within a range of less than 1 μm and the overall distribution features a 'concave' form. As the cumulative intrusive mercury saturation decreases, the percentage of saturation due to pore throats larger than 0.1 μm gradually decreases, from 59.11% of sample 6-1 to 15.68% of sample 4-7. The frequency of the relatively large pore throats

Table 1. Pore structure parameters of 25 tight sandstone samples from the Linxing block.

Sample number	Depth (m)	Porosity (%)	Air permeability (10^{-3} μm^2)	Average pore radius (μm)	r_{35} (μm)	Entry pressure (MPa)	Maximum S_{Hg} (%)	Efficiency of mercury withdrawal (%)	Classification of pore structure
1-9	1888.20	5.36	0.25	0.33	0.12	0.68	74.16	38.52	III
4-1	1562.60	9.55	0.11	0.14	0.08	1.36	84.83	37.70	III
4-2	1564.00	8.06	0.11	0.19	0.24	1.36	90.90	44.84	II
4-3	1573.40	9.16	0.25	0.40	0.28	0.47	86.50	29.41	II
4-4	1613.40	8.87	0.07	0.17	0.08	1.02	86.20	35.44	III
4-5	1593.69	7.70	0.11	0.16	0.05	1.02	72.31	33.59	III
4-6	1593.76	7.90	0.12	0.18	0.06	1.02	75.56	32.83	III
4-7	1594.34	4.62	0.05	0.15	0.01	1.37	39.83	43.63	IV
4-8	1595.26	5.14	0.06	0.15	0.01	1.37	46.46	39.21	IV
4-9	1596.19	8.52	0.21	0.25	0.11	0.67	78.27	34.09	III
5-1	1597.95	4.76	0.09	0.27	0.01	0.67	36.16	38.46	IV
5-2	1599.59	10.16	0.4	0.25	0.03	0.46	85.47	33.76	III
5-3	1599.97	9.20	1.96	0.54	0.01	0.33	40.84	27.20	IV
5-4	1600.50	8.34	0.14	0.19	0.06	0.68	81.68	35.35	III
5-5	1601.34	8.27	0.15	0.21	0.07	0.68	78.85	33.64	III
6-1	1648.69	10.06	0.72	0.56	0.69	0.33	96.83	33.60	I
6-2	1650.00	6.37	0.22	0.24	0.22	0.68	87.75	35.02	II
6-3	1646.20	9.95	0.15	0.24	0.22	0.68	91.95	30.63	II
6-4	1647.00	7.55	0.08	0.17	0.08	1.02	80.02	28.58	III
6-5	1649.02	8.93	0.46	0.62	0.79	0.33	93.25	32.54	I
7-1	1482.56	7.10	0.41	0.40	0.22	0.47	77.24	42.18	III
7-2	1515.48	12.70	0.81	0.51	0.44	0.33	93.10	28.53	I
7-3	1516.77	11.80	0.76	0.44	0.22	0.47	84.07	31.32	III
8-1	1658.60	8.28	0.14	0.17	0.23	1.36	91.24	46.94	II
9-1	1713.74	8.12	0.65	0.33	0.01	0.68	41.48	33.72	IV

Table 2. Classification of reservoir pore structure according to the capillary pressure curve.

Type of pore structure	Shape of the capillary pressure curve	Maximum S_{Hg} (%)	r_{35} (μm)	Porosity (%)
I	Coarse type	93.10 ~ 96.83	0.44 ~ 0.79	8.93 ~ 12.70
II	Partial coarse type	86.50 ~ 91.95	0.22 ~ 0.28	6.37 ~ 9.95
III	Partial fine type	72.31 ~ 86.20	0.03 ~ 0.22	5.36 ~ 11.80
IV	Fine type	36.16 ~ 46.46	0.01	4.62 ~ 9.20

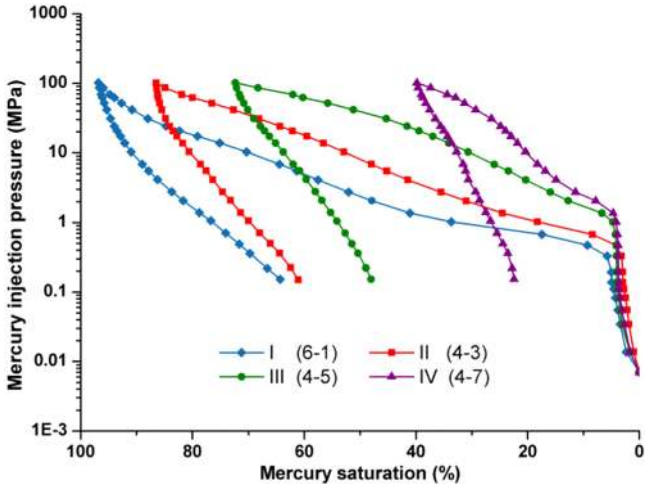

Figure 2. Typical capillary pressure curves of the Linxing block.

(>0.63 μm) also decreases gradually, which results in lowered porosity and permeability, as well as a worsening of the petrophysical properties (figure 3). In general, the pore structures in the research area are complicated, and they deteriorate from type I to type IV, with type I being the most favorable for exploiting tight sandstone gas.

3.2. Fractal characteristics

Different methods (method I, method II and method III) have been derived to calculate the fractal dimension according to fractal theory and utilizing mercury intrusion porosimetry. Theoretically, these different methods have all been derived based on fractal theory, with the only differences arising from the derivation of the formulas. Each method is valid as long as the pore structure has fractal characteristics, which allows the use of the fractal dimension obtained by different methods to

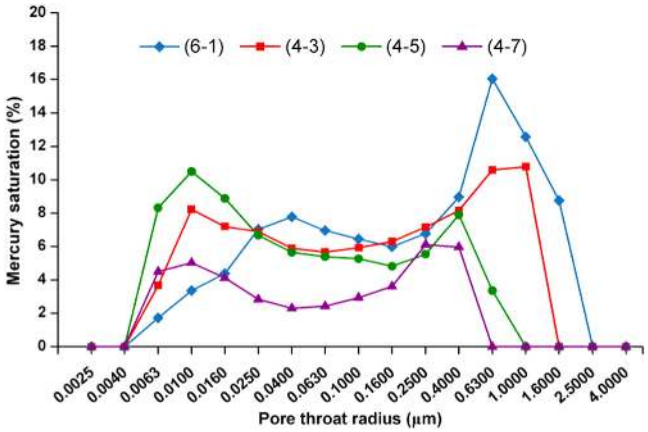

Figure 3. Line charts of pore throat size distribution for typical samples.

characterize the complexity of the pore structure. In the following text, the similarities and differences of the different methods are described in detail, using representative samples 6-1, 4-3, 4-5 and 4-7 as examples.

3.2.1. Fractal dimensions and fractal curves of typical samples. A double logarithmic plot of 1-S_{Hg} and P_c is used in method I. It can be seen that the fractal curves show an apparent three-section structure with good linearity, which indicates that different pore scales have different fractal characteristics (figure 4). First, the fractal dimensions of each section of the linear curve are obtained (denoted by D_{I1}, D_{I2} and D_{I3}). Then, weighted averaging of these fractal dimensions is performed based on the mercury saturation percentage that the pores of these three sections account for, and finally, the fractal dimension characterizing the general pore structure can be obtained (denoted by D_I) (table 3).

With method II, a double logarithmic plot of S_{Hg} and P_c is made. It can be seen that there are abrupt fluctuations and generally fewer data points ($2 \sim 3$) in the middle section of the fractal curves, but they still show overall linearity (figure 5). During the calculation of the fractal dimension, the overall linear fractal dimension is calculated (denoted by D_{II}), and the fractal dimensions of the other two sections, except for the middle section with fluctuations, are also calculated in table 3 (denoted by D_{II1} and D_{II3}).

The double logarithmic plot of dV_{Hg}/dP_c and P_c is used by method III. It can be seen that the features of the fractal curves obtained by this method are consistent with those of the double logarithmic curves plotted by method II. They also show abrupt fluctuations in the middle section, but overall, the curves are linear (figure 6).

Further analysis has revealed that methods II and III differ only in the selection of a simplified pore shape model. Pores are treated with the capillary bundle model in method II, while they are considered spheres in method III. In terms of calculation, the pore volume has a quadratic relationship with the pore radius in method II, while that same relationship is cubic in method III. Equation (19) may be obtained by taking the derivative of equation (17) in the same way as that of equations (15) and (16). It is apparent that the fractal dimensions obtained by equations (19) and (16) will differ by 1. This explains why the fractal dimensions calculated by

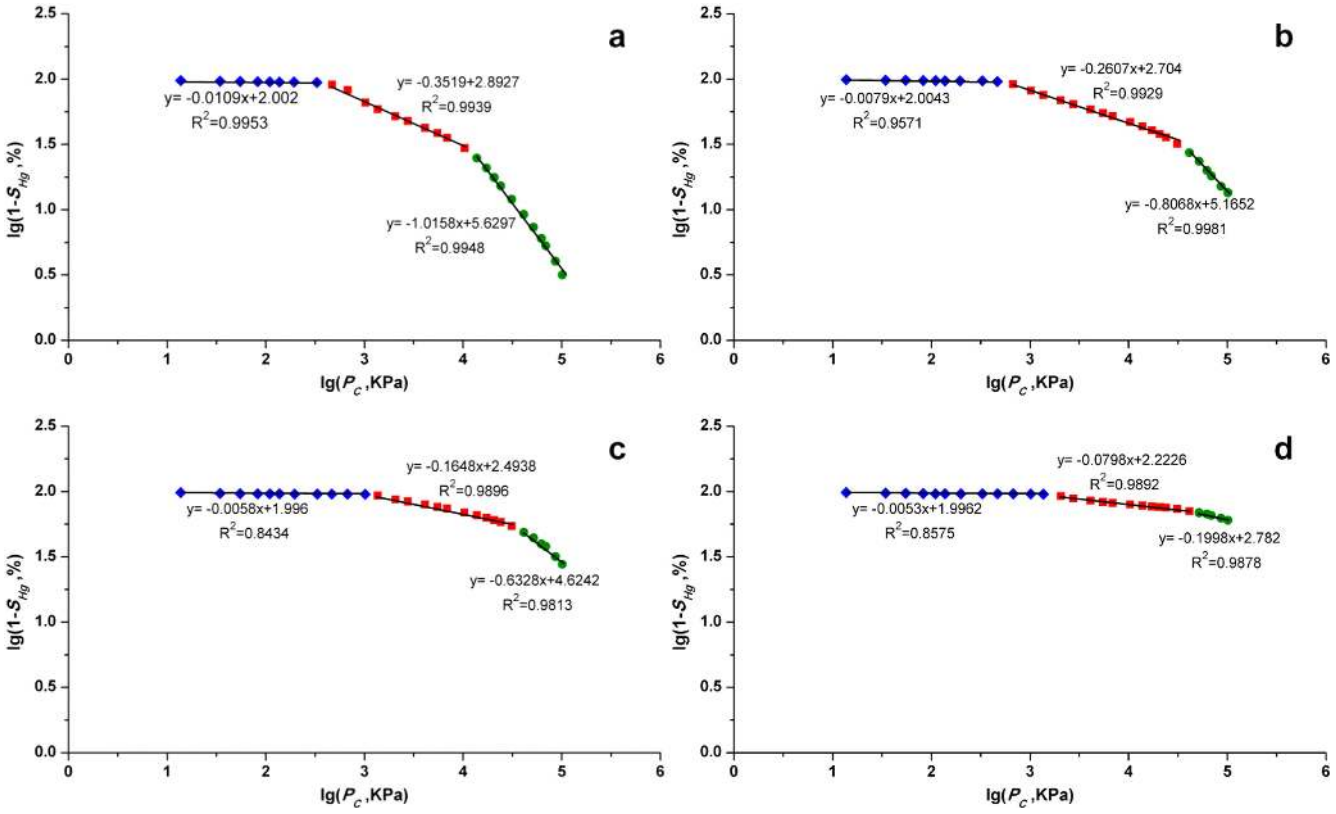

Figure 4. Fractal curves of typical samples plotted by method I. (a) Sample 6-1, (b) sample 4-3, (c) sample 4-5, (d) sample 4-7.

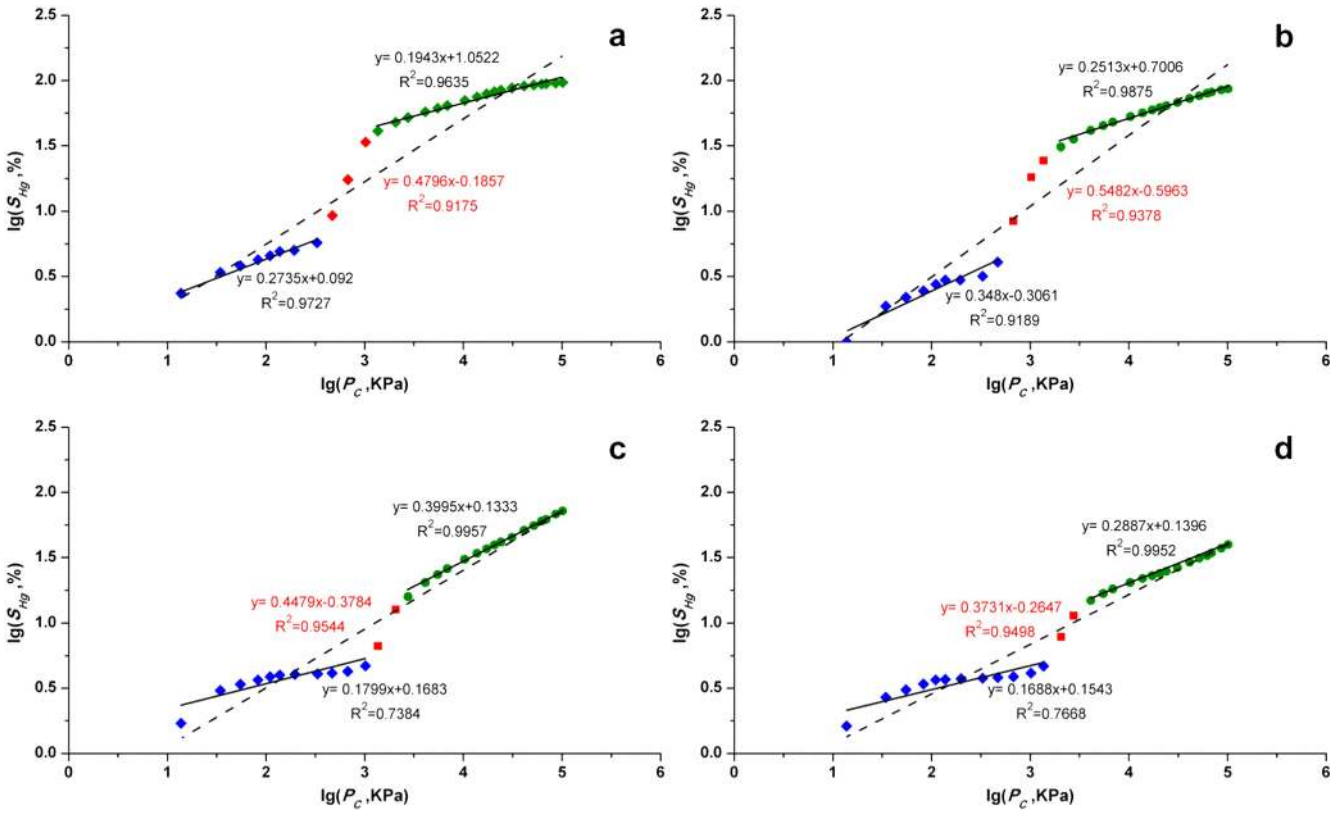

Figure 5. Fractal curves of typical samples plotted by method II (the dotted curve and the red linear fitting formula show overall linearity). (a) Sample 6-1, (b) sample 4-3, (c) sample 4-5, (d) sample 4-7.

Table 3. Fractal dimensions of different methods for 25 samples from the Linxing block.

	Method I				Method II			Method III
Sample number	D_{I1}	D_{I2}	D_{I3}	D_{I}	D_{II1}	D_{II3}	D_{II}	D_{III}
1-9	2.99	2.88	2.17	2.67	2.23	2.26	2.42	3.42
4-1	3.00	2.80	1.95	2.46	2.56	2.40	2.56	3.56
4-2	3.00	2.54	2.22	2.50	2.13	2.21	2.57	3.57
4-3	2.99	2.80	2.19	2.64	2.35	2.25	2.55	3.55
4-4	2.99	2.81	1.98	2.45	2.23	2.40	2.55	3.55
4-5	2.99	2.84	2.37	2.67	2.18	2.40	2.45	3.45
4-6	2.99	2.82	2.18	2.64	2.18	2.37	2.45	3.45
4-7	2.99	2.92	2.80	2.90	2.17	2.29	2.37	3.37
4-8	2.99	2.91	2.72	2.86	2.21	2.28	2.39	3.39
4-9	3.00	2.80	2.27	2.56	2.18	2.32	2.52	3.52
5-1	2.99	2.93	2.85	2.92	2.22	2.26	2.37	3.37
5-2	3.00	2.89	1.77	2.24	2.28	2.48	2.54	3.54
5-3	2.99	2.95	2.66	2.87	2.45	2.24	2.36	3.36
5-4	2.99	2.84	2.13	2.52	2.17	2.43	2.45	3.45
5-5	3.00	2.82	2.23	2.62	2.19	2.39	2.51	3.51
6-1	2.99	2.65	1.90	2.46	2.27	2.19	2.48	3.48
6-2	2.98	2.62	2.38	2.62	2.36	2.28	2.52	3.52
6-3	2.99	2.62	1.94	2.52	2.27	2.28	2.52	3.52
6-4	2.99	2.81	1.90	2.54	2.21	2.33	2.43	3.43
6-5	2.99	2.64	2.38	2.59	2.32	2.17	2.49	3.49
7-1	2.99	2.86	2.36	2.68	2.28	2.22	2.44	3.44
7-2	2.99	2.67	2.05	2.57	2.27	2.24	2.54	3.54
7-3	2.99	2.82	2.31	2.64	2.34	2.28	2.49	3.49
8-1	2.99	2.50	2.15	2.47	2.20	2.21	2.59	3.59
9-1	2.99	2.96	2.73	2.87	2.23	2.20	2.36	3.36

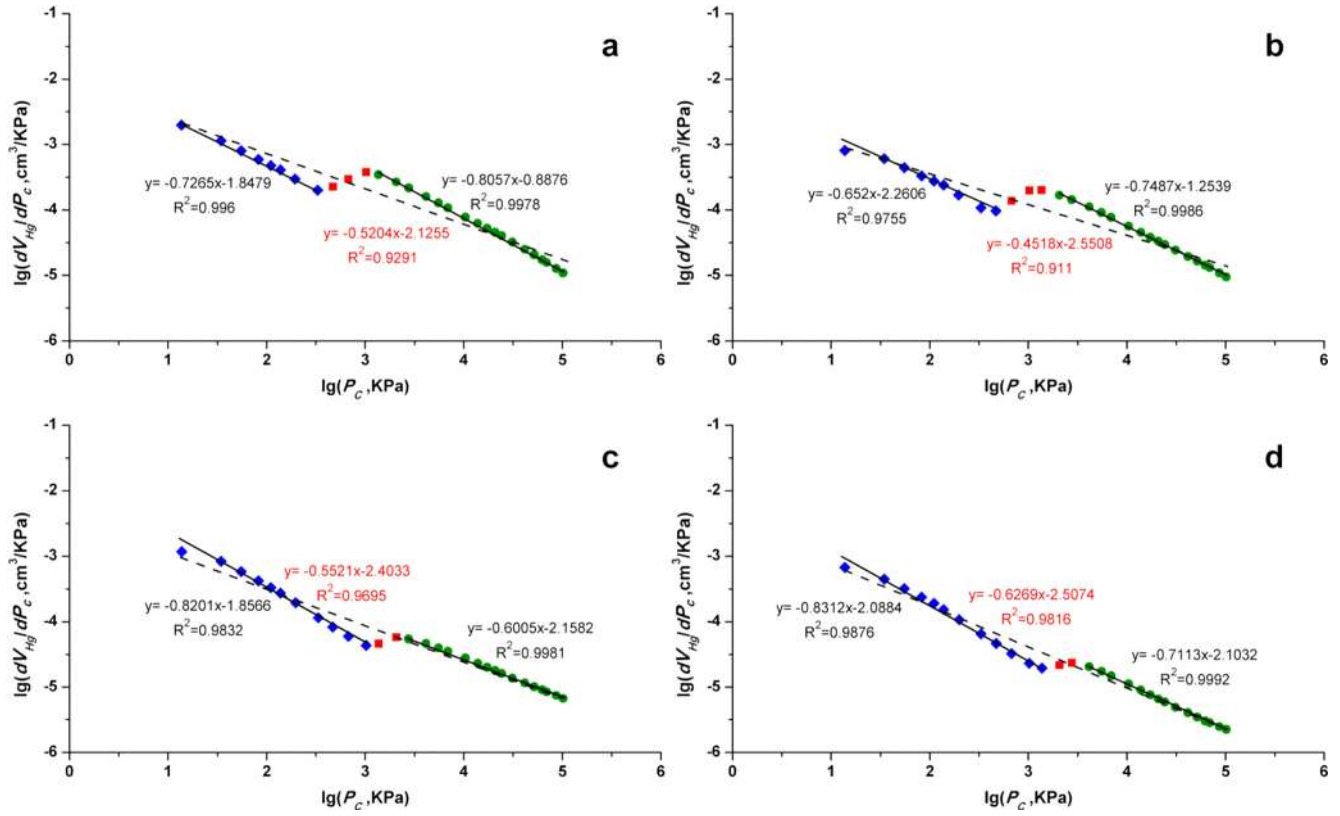

Figure 6. Fractal curves of typical samples plotted by method III (the dotted curve and the red linear fitting formula show overall linearity). (a) Sample 6-1, (b) sample 4-3, (c) sample 4-5, (d) sample 4-7.

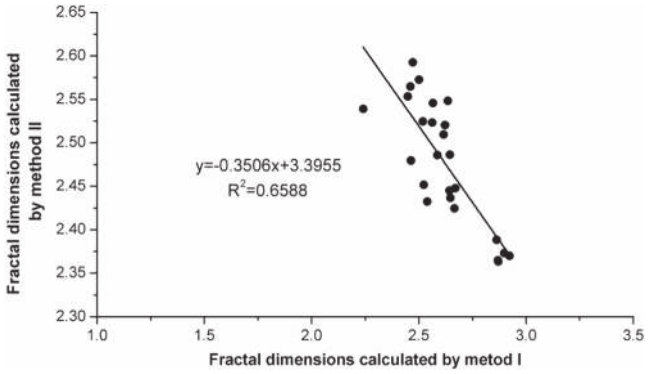

Figure 7. Plot showing the relationship between fractal dimensions calculated by methods I and II.

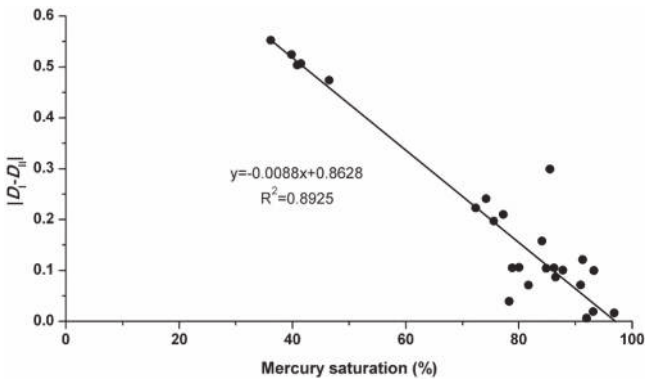

Figure 8. Plots of $|D_{\mathrm{I}}\text{-}D_{\mathrm{II}}|$ versus mercury saturation.

method III are within the range of $3 \sim 4$ (table 3). Therefore, one cannot simply judge that the pore structure does not have fractal characteristics just because the values of the fractal dimension are not within the range of $2 \sim 3$. The judgment should be made after checking whether the calculated values are consistent with fractal theory. For the three methods mentioned in this paper, as long as the fractal curves show apparent linearity, the pore structure will have fractal characteristics:

$$S_{\mathrm{Hg}} = \alpha P_{\mathrm{c}}^{-(3-D)}. \tag{19}$$

Fractal dimensions have been obtained by the three methods mentioned above. The fractal curves demonstrate linearity both in separate sections and combined, indicating that the pore structure of the tight sandstone reservoir in the He 8 member of the Linxing block has fractal characteristics. However, different computing methods result in different fractal dimensions (table 3). As methods II and III are actually the same, the following text analyzes only the theoretical difference between methods I and II and the suitability of each fractal dimension for reflecting the characteristics of the pore structure.

During the process to calculate the fractal dimension using method I, it is assumed that $r_{\min} \ll r_{\max}$ and r to simplify the calculation process. The maximum mercury injection pressure of the porosity analyzer used was 101.32 MPa, which reflects a minimum pore radius of 7.25×10^{-3} μm and meets the assumed conditions. With method I, the fractal

Table 4. Inflection parameters of 25 samples from the Linxing block.

	Method I				Method II					
	First inflexion		Second inflexion		First inflexion		Second inflexion		Plots of mercury saturation/ injection pressure versus mercury saturation	
Sample number	P_c (MPa)	r (μm)	P_c (MPa)	r (μm)	P_c (MPa)	r (μm)	P_c (MPa)	r (μm)	Minimum point pore radius	Maximum point pore radius
1-9	0.68	1.08	41.35	0.02	0.68	1.08	1.02	0.72	1.08	0.72
4-1	1.36	0.54	31.00	0.02	1.36	0.54	4.13	0.18	0.54	0.18
4-2	1.02	0.72	24.11	0.03	1.02	0.72	2.75	0.27	0.72	0.27
4-3	0.47	1.57	31.00	0.02	0.47	1.57	1.36	0.54	1.57	0.54
4-4	1.02	0.72	24.11	0.03	1.02	0.72	2.74	0.27	0.72	0.27
4-5	1.02	0.72	31.00	0.02	1.02	0.72	2.06	0.36	0.72	0.36
4-6	1.02	0.72	41.35	0.02	1.02	0.72	2.06	0.36	0.72	0.36
4-7	1.37	0.54	41.34	0.02	1.37	0.54	2.75	0.27	0.54	0.27
4-8	1.37	0.54	41.34	0.02	1.37	0.54	2.75	0.27	0.54	0.27
4-9	0.67	1.10	31.00	0.02	0.67	1.10	2.05	0.36	1.10	0.36
5-1	0.67	1.10	41.35	0.02	0.67	1.10	1.36	0.54	1.10	0.54
5-2	0.46	1.58	24.11	0.03	0.46	1.58	1.02	0.72	1.58	0.72
5-3	0.33	2.24	51.69	0.01	0.33	2.24	0.46	1.59	2.24	1.59
5-4	1.02	0.72	24.10	0.03	1.02	0.72	2.06	0.36	0.72	0.36
5-5	0.68	1.09	31.00	0.02	0.68	1.09	2.06	0.36	1.09	0.36
6-1	0.33	2.23	10.34	0.07	0.33	2.23	1.02	0.72	2.23	0.72
6-2	1.03	0.72	31.00	0.02	1.03	0.72	2.06	0.36	0.72	0.36
6-3	0.68	1.09	31.00	0.02	0.68	1.09	2.06	0.36	1.09	0.36
6-4	1.37	0.54	41.34	0.02	1.37	0.54	2.74	0.27	0.54	0.27
6-5	0.33	2.24	6.88	0.11	0.33	2.24	1.02	0.72	2.24	0.72
7-1	0.47	1.58	24.11	0.03	0.47	1.57	1.02	0.72	0.47	1.02
7-2	0.47	1.58	24.10	0.03	0.47	1.58	1.01	0.72	1.58	0.72
7-3	0.47	1.57	20.66	0.04	0.47	1.57	1.02	0.72	1.57	0.72
8-1	1.36	0.54	30.99	0.02	1.36	0.54	4.11	0.18	0.54	0.18
9-1	0.67	1.09	31.00	0.02	0.67	1.09	1.02	0.72	1.09	0.72

dimension is obtained using the relationship between the wetting phase saturation and injection pressure. What is actually calculated is the pores not intruded by mercury at a certain pressure. With method II, the fractal dimension is acquired using the relationship between the non-wetting phase saturation and injection pressure, and the fractal dimension of the pores intruded by mercury at a certain pressure is being calculated. The theoretical difference between these two methods directly results in the differences in the fractal curves and calculation results.

As the non-wetting phase, S_{Hg}, gradually increases and the wetting phase, 1-S_{Hg}, gradually decreases during the mercury intrusion porosimetry measurement, the fractal curves calculated by method I show a declining trend with a negative slope (figure 4), whereas the fractal curves calculated by method II show an increasing trend with a positive slope (figure 5). In addition, due to the inverse relationship between the wetting phase and non-wetting phase, the fractal dimensions calculated by methods I and II are negatively correlated (figure 7). The fractal dimensions calculated by method I for the remaining pores include pores which the mercury cannot intrude at the maximum test pressure, as well as isolated or enclosed pores. Therefore, when the intrusive mercury saturation is relatively low, the fractal dimension calculated by this method is very different from that calculated by method II (table 3, figure 8).

The fractal dimensions of the separate sections calculated by method I decrease gradually ($D_{I1} > D_{I2} > D_{I3}$), indicating that the heterogeneity of the remaining pores becomes weaker. As the petrophysical properties deteriorate, the fractal dimensions of the separate sections and of the entirety will increase gradually ($D_{I(6\text{-}1)} < D_{I(4\text{-}3)} < D_{I(4\text{-}5)} < D_{I(4\text{-}7)}$). The fractal curves tend to gradually change from three sections to one section, indicating that the pore distribution is becoming homogeneous and the reservoir is mainly composed of micropores (figure 4). A great number of micropores in the reservoir leads to low porosity and permeability, so the connectivity of the reservoir is mainly affected by large pores. Although the fractal curves obtained by method II show linearity overall, there are two apparent turning points. The fractal curve section before the first turning point and after the second turning point demonstrate good linearity, with the fractal curves after the second turning point being more linear (figure 5), an indication that if the pore radius is less than a certain value ($<0.27 \sim 1.59\,\mu$m), the pore structures will have relatively uniform features and strong self-similarity.

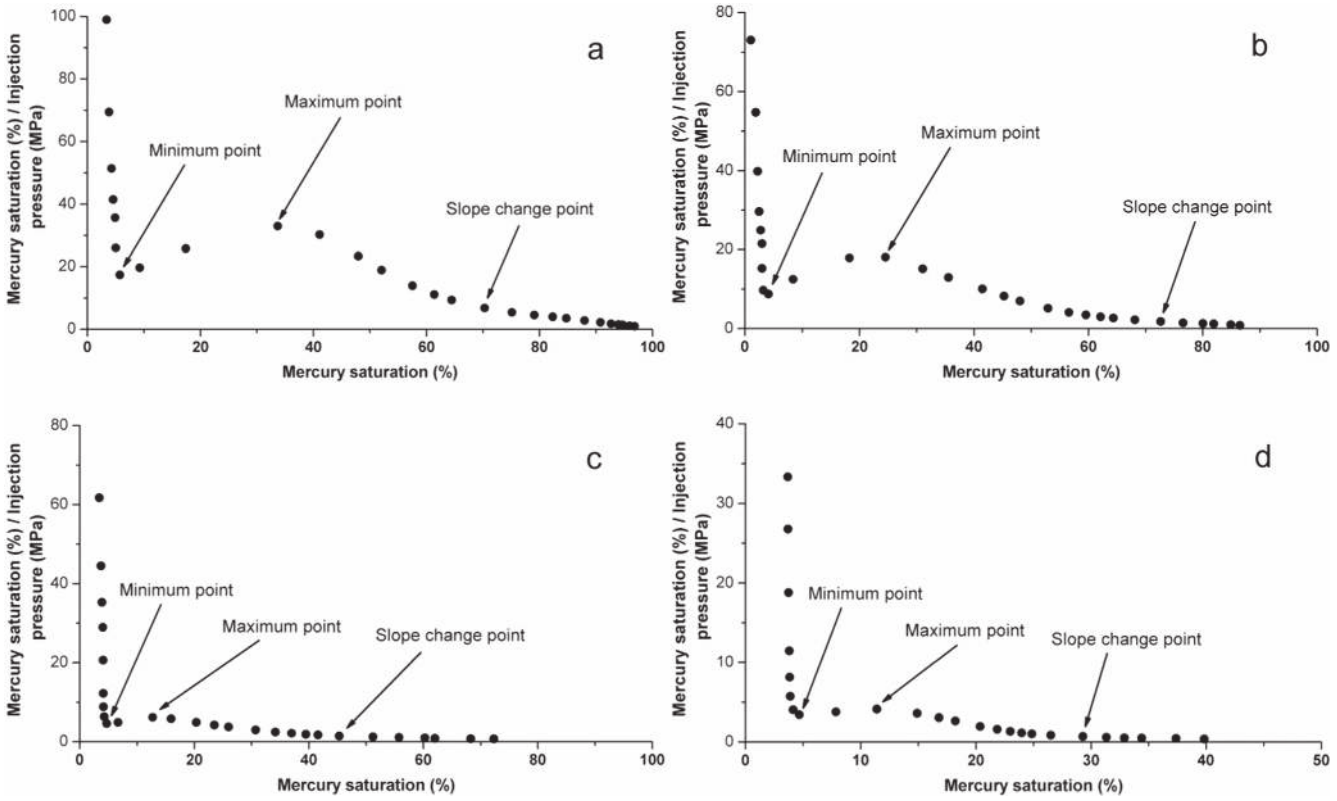

Figure 9. Plots of mercury saturation/injection pressure versus mercury saturation for typical samples. (a) Sample 6-1, (b) sample 4-3, (c) sample 4-5, (d) sample 4-7.

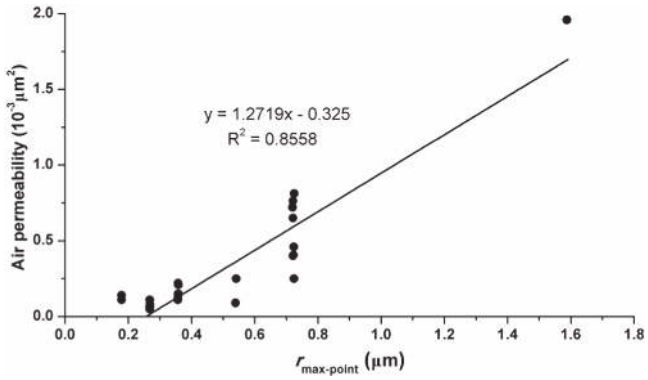

Figure 10. Diagram of air permeability plotted against $r_{\text{max-point}}$.

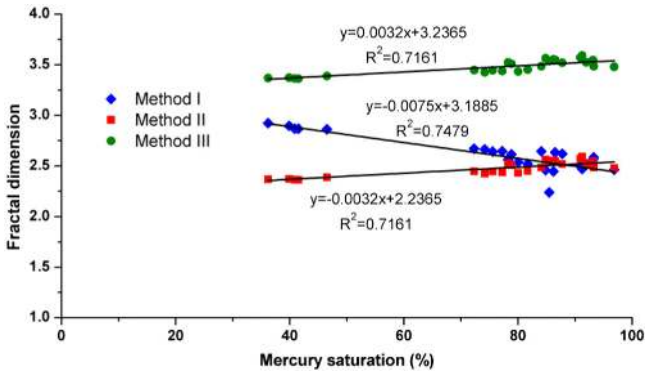

Figure 11. Plots of fractal dimension versus mercury saturation.

3.2.2. Relationship between morphology and the fractal curves derived from different methods. Through statistical analysis, it has been found that there is a consistency between the turning points of the fractal curves obtained with the different methods (table 4). The first turning points of the fractal curves are completely identical between the three different methods. The second turning points of the method II and method III curves are also identical, as expected, because they are actually the same method. For further analysis, scatter diagrams of mercury saturation/injection pressure and mercury saturation were plotted. Unlike the single peak plots of Lai and Wang (2015), these scatter diagrams present an inverse S shape with two obvious inflections, including a minimum point and a maximum point. After the changing trend of the scatter diagrams were analyzed, it was found that there is an apparent slope change after the maximum point (figure 9). The analysis also revealed that the minimum points correspond with the first turning points on the fractal curves, the maximum points correspond with the second tuning points on the fractal curves from methods II and III, and the point where the slope changes corresponds with the second turning points on the fractal curves obtained by method I. In fact, the amount of mercury injected is very small before the minimum point, indicating that there are fewer large pores distributed in the tight sandstone reservoir. The mercury starts to enter the pores in a large amount after the minimum point, resulting in the transition on the mercury intrusion curves and the fractal curves. The maximum point is actually the same as the apex described in the papers of Nabawy *et al* (2009) and

Lai and Wang (2015). Figure 10 shows a scatter plot of the $r_{max\text{-}point}$ (the pore radius corresponding to the maximum point) and the air permeability. There is a positive correlation between the $r_{max\text{-}point}$ and air permeability, in agreement with Lai and Wang (2015) and indicating the transition from broad and well-connected pores to small and poorly-connected pores. After the maximum point, the pore structures of methods II and III show apparent and uniform fractal characteristics. Method I is different in that the second turning points of the fractal curves correspond to the points where the slope changes. This is mainly because method I calculates the fractal dimensions of the remaining pores, which, due to the nature of the logarithms, changes more as the value becomes less. Therefore, when the pore radius is relatively small, the value of $\lg(1\text{-}S_{Hg})$ will change significantly, even for small changes in intrusive mercury saturation.

In general, the fractal curves and fractal dimensions obtained by the different methods vary greatly. The correlation between the overall fractal dimensions obtained by the three methods and the structural parameters of the pores is not significant, except during maximum mercury saturation. However, the fractal dimensions obtained by method I are negatively correlated with the maximum mercury saturation and gradually increase as the petrophysical properties deteriorate (figure 11). This indicates that method I is a better method for describing the complexity and petrophysical properties of the pore structure in the study area. Methods II and III obtain the fractal dimensions via the relation between intrusive mercury saturation and injection pressure, but tight sandstone reservoirs are normally composed of micropores. The amount of mercury entering the pores is much less before the minimum point, then increases abruptly between the minimum point and the maximum point. These changes greatly affect the calculation of the fractal dimension.

4. Conclusions

Based on the present work, the following conclusions may be drawn:

1. The tight sandstone reservoir of the He 8 member in the Linxing block contains complex pore structures which can be divided into four types. The pore structures and petrophysical properties deteriorate from type I to type IV, with type I being the most favorable for the exploitation of tight sandstone gas.
2. The fractal characteristics of a reservoir should be determined based on whether fractal curves have linear features, and different pore scales have different fractal characteristics. The fractal dimension obtained by method I, which describes the fractal characteristics of the remaining pores, is more suitable for describing the complexity and petrophysical properties in the Linxing block. Methods II and III both represent the pores intruded by mercury where the only difference is the selection of the simplified pore shape model.
3. The fractal curves obtained by the three methods have different characteristics. The fractal curves plotted by method I have three distinct sections, while that plotted by methods II and III are mainly linear overall. The turning points of the fractal curves obtained by the three methods appear to correspond with minimum points, maximum points and points where the slope changes. Small pores ($<r_{max\text{-}point}$) usually present more obvious fractal characteristics, while large pores ($>r_{max\text{-}point}$) are the key factor controlling reservoir seepage characteristics.

Acknowledgments

This work was supported by the National Major Special Project of Science and Technology of China (2016ZX05044001), the Natural Science Foundation of China (41272178, 41572140), the Fundamental Research Funds for the Central Universities (2014ZDPY26, 2015XKZD07), and the Qing Lan Project.

References

Angulo R F and Gonzalez H 1992 Fractal dimensions from mercury intrusion capillary tests *SPE* **23695** 255–63
Burdine N T 1953 Relative permeability calculation from size distribution data *J. Pet. Technol.* **5** 71–8
Clarkson C R, Freeman M, He L, Agamalian M, Melnichenko Y B, Mastalerz M, Bustin R M, Radliński A P and Blach T P 2012 Characterization of tight gas reservoir pore structure using USANS/SANS and gas adsorption analysis *Fuel* **95** 371–85
Friesen W I and Mikula R J 1987 Fractal dimensions of coal particles *J. Colloid. Interface Sci.* **120** 263–71
Fu X H, Qin Y, Zhang W N, Wei C T and Zhou R F 2005 Fractal classification and natural classification of coal pore structure based on migration of coal bed methane *Chin. Sci. Bull.* **50** 66–71
Gao Z Y and Hu Q H 2013 Estimating permeability using median pore-throat radius obtained from mercury intrusion porosimetry *J. Geophys. Eng.* **10** 025014
Guo J F, Xie R H, Zou Y L and Ding Y J 2016 Numerical simulation of multi-dimensional NMR response in tight sandstone *J. Geophys. Eng.* **13** 285–94
He C and Hua M 1998 Fractal geometry description of reservoir pore structure *Oil & Gas Geol.* **19** 15–23 (in Chinese)
Holditch S A 2006 Tight gas sands *J. Pet. Technol.* **58** 84–90
Jiang Z X, Li Z, Li F, Pang X Q, Yang W, Liu L F and Jiang F J 2015 Tight sandstone gas accumulation mechanism and development models *Pet. Sci.* **12** 587–605
Katz A J and Thompson A H 1985 Fractal sandstone pores: implications for conductivity and pore formation *Phys. Rev. Lett.* **54** 1325–8
Krohn C E 1988a Fractal measurements of sandstones, shales, and carbonates *J. Geophys. Res.* **93** 3297–305
Krohn C E 1988b Sandstone fractal and euclidean pore volume distributions *J. Geophys. Res.* **93** 3286–96
Lai J and Wang G 2015 Fractal analysis of tight gas sandstones using high-pressure mercury intrusion techniques *J. Nat. Gas. Sci. Eng.* **24** 185–796

León y León C A 1998 New perspectives in mercury porosimetry *Adv. Colloid Interface Sci.* **76-77** 341–72

Li K 2010 Analytical derivation of Brooks-Corey type capillary pressure models using fractal geometry and evaluation of rock heterogeneity *J. Pet. Sci. Eng.* **73** 20–6

Li K W and Horne R N 2003 Fractal characterization of the geysers rock *GRC Trans.* **27** 1–8

Li K W and Horne R N 2006 Fractal modeling of capillary pressure curves for The Geysers rocks *Geothermics* **35** 198–207

Li Y, Lu G and Rudolph V 1999 Compressibility and fractal dimension of fine coal particles in relation to pore structure characterisation using mercury porosimetry *Part. Part. Syst. Charact.* **16** 25–31

Morad S, Al-Ramadan K, Ketzer J M and Ros L F D 2010 The impact of diagenesis on the heterogeneity of sandstone reservoirs: a review of the role of depositional facies and sequence stratigraphy *AAPG Bull.* **94** 1267–309

Nabawy B S, Géraud Y, Rochette P and Bur N 2009 Pore-throat characterization in highly porous and permeable sandstones *AAPG Bull.* **93** 719–39

Pérez Bernal J L and Bello López M A 2000 The fractal dimension of stone pore surface as weathering descriptor *Appl. Surf. Sci.* **161** 47–53

Pfeifer P and Avnir D 1983 Chemistry in nonintegral dimensions between two and three *J. Chem. Phys.* **79** 3369–558

Shen P P, Li K W and Jia F S 1995 Quantitative description for the heterogeneity of pore structure by using mercury capillary pressure curves *SPE* **29996** 447–56

Wong P, Howard J and Lin J S 1986 Surface roughening and the fractal nature of rocks *Phys. Rev. Lett.* **57** 637–40

Xiao L, Zou C C, Mao Z Q, Jin Y, Shi Y J, Guo H P and Li G R 2016 An empirical approach of evaluating tight sandstone reservoir pore structure in the absence of NMR logs *J. Pet. Sci. Eng.* **137** 227–39

Xie K C, Qiu Z J, Jin Q H, Yuan L and Zhao W Z 2014 *Strategic Research of Unconventional Gas Development and Utilization in China* (Beijing: Science Press) pp 96–9 (in Chinese)

Yang F, Ning Z F and Liu H Q 2014 Fractal characteristics of shales from a shale gas reservoir in the Sichuan Basin, China *Fuel* **115** 378–84

Yao Y B, Liu D M, Tang D Z, Tang S H, Huang W H, Liu Z H and Che Y 2009 Fractal characterization of seepage-pores of coals from China: an investigation on permeability of coals *Comput. Geosci.* **35** 1159–66

Zhu P, Lin C, Ren H, Zhao Z and Zhang H 2015 Micro-fracture characteristics of tight sandstone reservoirs and its evaluation by capillary pressure curves: a case study of Permian sandstones in Ordos Basin, China *J. Nat. Gas Sci. Eng.* **27** 90–7

Ziarani A S and Aguilera R 2012 Pore-throat radius and tortuosity estimation from formation resistivity data for tight-gas sandstone reservoirs *J. Appl. Geophys.* **83** 65–73

Zou C N, Zhu R K, Liu K Y, Su L, Bai B, Zhang X X, Yuan X J and Wang J H 2012 Tight gas sandstone reservoirs in China: characteristics and recognition criteria *J. Pet. Sci. Eng.* **88-89** 82–91